

# Microlithography of hole transport layers for high-resolution organic light-emitting diodes with reduced electrical crosstalk

Received: 9 December 2023

Accepted: 29 November 2024

Published online: 27 January 2025

 Check for updates

Hyukmin Kweon<sup>1,7,8</sup>, Seonkwon Kim<sup>2,8</sup>, Borina Ha<sup>1,8</sup>, Seunghan Lee<sup>3</sup>, Soyeon Lee<sup>1</sup>, SeungHwan Roh<sup>3</sup>, Hayoung Oh<sup>1</sup>, Jiyeon Ha<sup>1</sup>, Minsu Kang<sup>2</sup>, Moon Sung Kang<sup>3,4</sup>✉, Jeong Ho Cho<sup>2</sup>✉ & Do Hwan Kim<sup>1,5,6</sup>✉

High-density displays are required for the development of virtual and augmented reality devices. However, increasing the pixel resolution can lead to higher electrical pixel crosstalk, primarily due to a shared hole transport layer. Here we show that a silicone-integrated small-molecule hole transport layer can be patterned at the wafer scale with microlithography to mitigate electrical pixel crosstalk. This provides high-density pixelation and improved performance of the hole transport layer itself. With this approach, we create high-fidelity micro-pattern arrays with a resolution of up to 10,062 pixels per inch on a six-inch wafer. The silicone-integrated small-molecule hole transport layer can effectively modulate charge balance within the emission layers, improving the luminance characteristics of organic light-emitting diodes. We also show that organic light-emitting diodes integrated with micro-patterned silicone-integrated small-molecule hole transport layers have a reduced electrical pixel crosstalk compared with organic light-emitting diodes with a typical hole transport layer.

Virtual and augmented reality devices can provide immersive experiences and enhance human–machine interactions by seamlessly combining the real and virtual worlds<sup>1–3</sup>. These devices require the integration of high-pixel-density microdisplays, and the technology has helped drive the development of high-resolution organic light-emitting diode (OLED) microdisplays with pixel densities of over 3,000 pixels per inch (ppi)<sup>2–5</sup> (Supplementary Fig. 1). However, as the pixel resolution increases, electrical pixel crosstalk can lead to a deterioration in both colour gamut and colour purity<sup>6,7</sup>. Therefore, high-resolution OLEDs require advanced pixel patterning processes, as well as methods to suppress crosstalk between neighbouring pixels at close proximity (Fig. 1a).

Electrical pixel crosstalk mainly originates from the use of a shared hole transport layer (HTL), which creates a conductive pathway allowing holes injected into active pixels to migrate to neighbouring non-active pixels<sup>6–9</sup> (Fig. 1b and Supplementary Note 1). HTLs with increased thickness or low doping levels have been developed to reduce parasitic charge flow from active to adjacent non-active pixels<sup>10,11</sup>. However, such approaches inevitably increase the driving voltage of displays<sup>7</sup>. Moreover, the leakage current tends to become more severe as the pixel resolution increases due to reduced pixel-to-pixel separation. A more fundamental way to suppress electrical crosstalk would be by directly pixelating the HTL in alignment with the subpixel resolution of the emission layer (EML) (Fig. 1c).

<sup>1</sup>Department of Chemical Engineering, Hanyang University, Seoul, Republic of Korea. <sup>2</sup>Department of Chemical and Biomolecular Engineering, Yonsei University, Seoul, Republic of Korea. <sup>3</sup>Department of Chemical and Biomolecular Engineering, Sogang University, Seoul, Republic of Korea. <sup>4</sup>Institute of Emergent Materials, Sogang University, Seoul, Republic of Korea. <sup>5</sup>Institute of Nano Science and Technology, Hanyang University, Seoul, Republic of Korea. <sup>6</sup>Clean-Energy Research Institute, Hanyang University, Seoul, Republic of Korea. <sup>7</sup>Present address: Department of Chemical Engineering, Stanford University, Stanford, CA, USA. <sup>8</sup>These authors contributed equally: Hyukmin Kweon, Seonkwon Kim, Borina Ha. ✉e-mail: [kangms@sogang.ac.kr](mailto:kangms@sogang.ac.kr); [jhcho94@yonsei.ac.kr](mailto:jhcho94@yonsei.ac.kr); [dhkim76@hanyang.ac.kr](mailto:dhkim76@hanyang.ac.kr)

A range of patterning techniques for small-molecule organic semiconductors (s-OSCs)—which are commonly used HTL materials<sup>12</sup>—have been explored, including transfer printing<sup>13–15</sup>, inkjet printing<sup>16,17</sup>, template growth<sup>18,19</sup>, fine metal mask<sup>20–22</sup> and photolithography<sup>23–25</sup> (Supplementary Table 1). Among the various techniques, fine metal mask and photolithography are arguably the most promising for achieving the high-resolution patterning needed for OLED microdisplays. A fine metal mask is widely adopted for patterning s-OSCs, with resolutions now reaching up to 3,000 ppi (ref. 22). However, challenges such as manufacturing yield, throughput concerns and mask deformation (which affects reusability and pattern accuracy) persist<sup>26,27</sup>. Photolithography, on the other hand, has expanded its micro-patterning capabilities to OLEDs. Adapting photolithography to fragile OLED materials require preventing molecular damage from the harsh environment of the photolithographic patterning process, such as exposure to chemicals or etching. To address this, we previously showed that OSCs formed in a semi-interpenetrating network structure by using a ladder-like silicone network creates films with chemical and physical robustness, enabling ultrahigh-resolution patterning of OSCs with conventional photolithography<sup>28</sup>. However, this strategy is only applicable to polymer semiconductors that have less practical usage in the display industry.

In addition to patterning capabilities, it is important that HTL materials can effectively transport charges and inject them into the EML, to maintain charge balance within the EML. To achieve this, efforts have been made to modulate the charge transport properties<sup>29–31</sup> and engineer the energy levels<sup>32–34</sup>, such as by shifting the highest occupied molecular orbital (HOMO) level or adopting multi-HTL structures. These approaches can enhance the HTL characteristics, but they cannot simultaneously address the high-density pixelation problem.

In this article, we show that wafer-scale microlithography in s-OSCs can mitigate pixel crosstalk in high-density micro-OLEDs. We create a silicone-integrated HTL (SI-HTL) by directly incorporating silicone blocks (Si–O–Si) into s-OSC molecules through covalent bonding. The SI-HTL can undergo micro-patterning using conventional photolithography and reactive ion etching (RIE), similar to conventional silicon semiconductors. This enables anisotropic, high-resolution SI-HTL patterns with resolution as small as 1  $\mu\text{m}$ . Simultaneously, the charge transport capability and energy levels of SI-HTL can be controlled by adjusting the concentration of silicone blocks, resulting in improved light-emitting performance in OLEDs compared with using non-silicone-incorporated HTLs. We also confirm the suppression of electrical pixel crosstalk between OLED subpixels based on the micro-patterned SI-HTL.

## Material design and photolithographic micro-patterns of SI-HTL

To create the SI-HTL, we used a simultaneous crosslinking reaction between oxetane-based crosslinkable s-OSCs and oxetane-based silicone crosslinkers (Fig. 1d; Methods provides the detailed crosslinking procedures). Among the oxetane-based s-OSCs (Supplementary Fig. 2), we primarily utilized N4,N4'-bis(4-(6-((3-ethyloxetan-3-yl)-methoxy)-hexyloxy)phenyl)-N4,N4'-bis(4-methoxyphenyl) biphenyl-4,4'-diamine (QUPD) as a representative material for the demonstration of SI-HTL. The oxetane ring-opening and sol–gel reactions facilitated the covalent crosslinking of QUPD and the silicone crosslinkers, successfully leading to the in situ formation of a silicone network within the SI-HTL matrix. The integrated silicone network of SI-HTL plays a crucial role in generating a non-volatile etch inhibitor ( $\text{Si}_x\text{O}_y$ ) at the sidewall of the etched trench during RIE (Supplementary Fig. 3). Intrinsically, s-OSCs exhibit an isotropic etching behaviour, which is attributed to omnidirectional chemical etching reactions that produce volatile reactants; however, the  $\text{Si}_x\text{O}_y$  etch inhibitor can reduce the lateral etch rate ( $r_l$ ) by alleviating the horizontal chemical etching reactions, allowing the vertical etch rate ( $r_v$ )—accelerated by

ion bombardments—to become predominant<sup>28</sup>. This orthogonal etching direction leads to the development of anisotropic etching profiles ( $r_v \gg r_l$ ). The cross-sectional transmission electron microscopy (TEM) analysis revealed that the  $r_l$  value of SI-HTL was effectively mitigated compared with that of the crosslinked QUPD (X-HTL), resulting in the clearly anisotropic etching behaviour of SI-HTL (Fig. 1e and Supplementary Fig. 4). This photolithography-driven anisotropic patterning strategy is beneficial to implement precise micro-patterns irrespective of the dimensional form factors. Figure 1f and Supplementary Fig. 5 exhibited wafer-scale, high-resolution patterning of SI-HTL, achieving ultrahigh-density pixelation corresponding to 10,062 ppi. The demonstrated resolution surpasses those of previously developed patterning methods for s-OSCs (Fig. 1g and Supplementary Table 1). This indicates that the SI-HTL design, compatible with photolithography and RIE processes, can simultaneously achieve high-resolution and scalable fabrications.

## Molecular and etching characteristics of SI-HTL

To ensure the high patternability of SI-HTL, the aforementioned crosslinking reactions between QUPD and silicone crosslinkers should be successfully executed. The Fourier transform infrared spectrum of SI-HTL showed a distinct disappearance of the peak corresponding to oxetane groups at 978  $\text{cm}^{-1}$ , accompanied by an increase in the intensity of the other stretching peaks at 1,107  $\text{cm}^{-1}$  (Fig. 2a)<sup>35</sup>. This provided clear evidence that the oxetane ring-opening reactions of both QUPD and silicone crosslinkers were completely carried out. Concurrently, the silicone stretching vibrations corresponding to 1,060  $\text{cm}^{-1}$  and 1,039  $\text{cm}^{-1}$  (lateral and vertical stretching, respectively) became markedly prominent<sup>36</sup>, indicating that the silicone network in the SI-HTL matrix was well developed. The distribution of the silicone network within the SI-HTL films was confirmed using time-of-flight secondary ion mass spectrometry (TOF-SIMS). The  $\text{NH}^+$  and  $\text{Si}^+/\text{SiO}^+$  signals corresponding to QUPD and elements of the silicon network, respectively, were determined as a function of the ion etching time for both X-HTL and SI-HTL. As shown in Fig. 2b, the signal distributions of  $\text{Si}^+$  and  $\text{SiO}^+$  were identical to that of  $\text{NH}^+$  across the entire films. This implies that the silicone network was uniformly distributed within SI-HTL; therefore, the film morphology of SI-HTL was analogous to that of X-HTL without a noticeable increase in surface roughness (Supplementary Fig. 6). Owing to the integration of the silicone network, SI-HTL can simultaneously possess chemical and dry etching resistances, which are a prerequisite to utilize the photolithography and RIE processes, even in a small-molecule system (Fig. 2c and Supplementary Figs. 7 and 8). We note that simply forming an interpenetrating network structure (that is, a QUPD network entangled with a silicone network, instead of forming chemical bonds between silicone moieties and QUPD molecules) could also be a plausible method to introduce a silicone network into a QUPD film, which can impart the film with chemical and physical robustness needed to withstand conventional photolithography (Supplementary Fig. 9). However, the resulting QUPD film (interpenetrating network HTL) exhibited a deterioration in the charge transport characteristics, presumably because the insulating silicone network hinders intermolecular transport between the conjugated units of QUPD molecules (Supplementary Fig. 10 and Supplementary Note 2). By contrast, this was not the case for SI-HTL. Consequently, SI-HTL demonstrated enhanced etching tolerance due to the silicone included in the film, without degrading the transport characteristics of s-OSC as well as the OLED performance (detailed device performance is discussed later).

The dry etching resistance and anisotropic etching behaviour, originating from the integrated silicone network, enable SI-HTL to achieve more accurate, fine micro-patterns through the photolithography and RIE processes. The pattern fidelity of photolithographic micro-patterns of SI-HTL was statistically evaluated in terms of linewidth variation (LWV) and line-edge roughness (LER)<sup>37</sup> (Fig. 2d

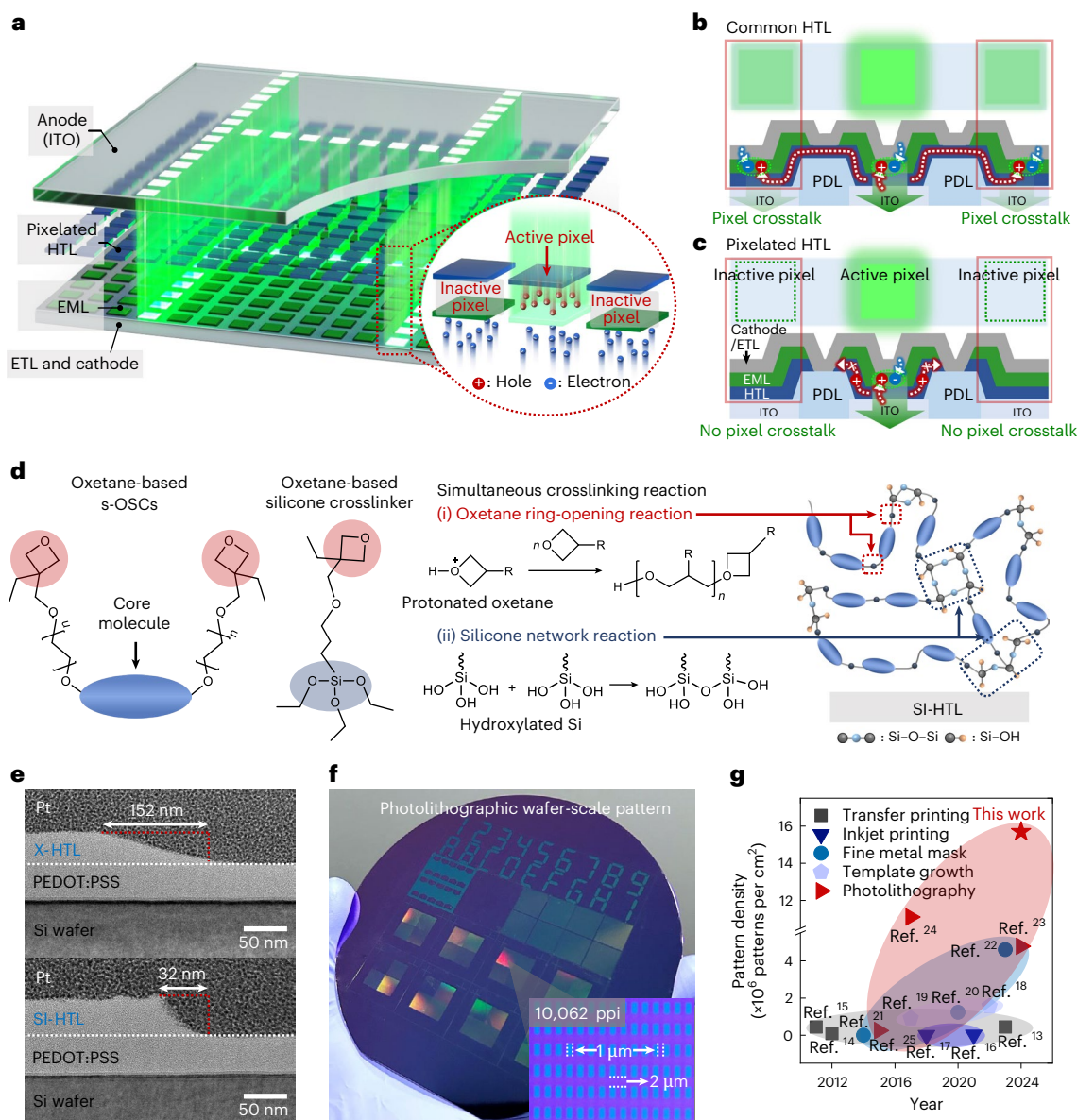


**Fig. 1 | Molecular concept and ultrahigh-density pixelation of SI-HTL.**

**a**, Schematic of high-resolution OLEDs with anti-pixel crosstalk. ETL, electron transport layer. **b,c**, Conceptual illustrations of electrical pixel crosstalk phenomenon depending on common HTL (**b**) and pixelated HTL (**c**). PDL, pixel define layer. **d**, Molecular structure and simultaneous crosslinking reaction

of SI-HTL. **e**, Cross-sectional TEM analysis of micro-patterns corresponding to X-HTL (top) and SI-HTL (bottom). **f**, Photograph of the wafer-scale fabrication of SI-HTL micro-pattern array achieved by photolithography and RIE processes. **g**, Comparisons with previously demonstrated pattern resolutions for s-OSCs (data from refs. 13–25).

and Supplementary Fig. 11). The LWV and LER values of patterns derived from SI-HTL were greatly reduced compared with those of X-HTL, resulting in the well-defined micro-patterns with high clarity. It is noteworthy that the silicone-driven high-resolution photolithography of HTLs could be readily achieved for various crosslinkable s-OSCs containing oxetane groups (Supplementary Fig. 12). This suggests the universal applicability of the patterning process based on the proposed silicone-integrated s-OSC films.

The demonstrated high-resolution and precise patterning results are attributed to the anisotropic etching mechanism of SI-HTL driven by silicone-based etch inhibitors. X-ray photoelectron spectroscopy (XPS) analysis was conducted to confirm the formation of etch inhibitors in SI-HTL depending on exposure to RIE. After RIE treatment on the SI-HTL film, the intensities of the  $\text{Si}2p$  peaks at 102.65 eV ( $\text{Si}^{3+}$  and  $\text{Si}_2\text{O}_3$ ) and 103.55 eV ( $\text{Si}^{4+}$  and  $\text{SiO}_2$ ) relatively increased compared with those at

100.75 eV ( $\text{Si}^0$  and  $\text{Si-O-Si}$ ) and 101.85 eV ( $\text{Si}^{2+}$  and  $\text{Si-O}$ ), causing a shift in the prominent main peak towards higher-binding-energy regions<sup>38,39</sup> (Fig. 2e and Supplementary Fig. 13). This means that the reactive gases ( $\text{O}^*$ ) effectively combined with the elements of the silicone network via chemical reactions, resulting in the formation of non-volatile Si suboxide reactants. Attributed to the etch inhibitor, chemical etching reactions (that is, the decomposition of organic compounds) on the surface of SI-HTL can be effectively suppressed (Supplementary Fig. 14). This retards the chemical-etching-induced reduction in molecular weight on the surface regime of SI-HTL films, which could affect the film modulus<sup>28,40</sup>. As shown in Fig. 2f, the decrease in the surface modulus for the SI-HTL film was less pronounced than that of the X-HTL film (the reduction rates of surface modulus were  $165 \text{ MPa s}^{-1}$  and  $238 \text{ MPa s}^{-1}$ , respectively) as the RIE exposure time increased (Supplementary Fig. 15). Consequently, these findings indicate that



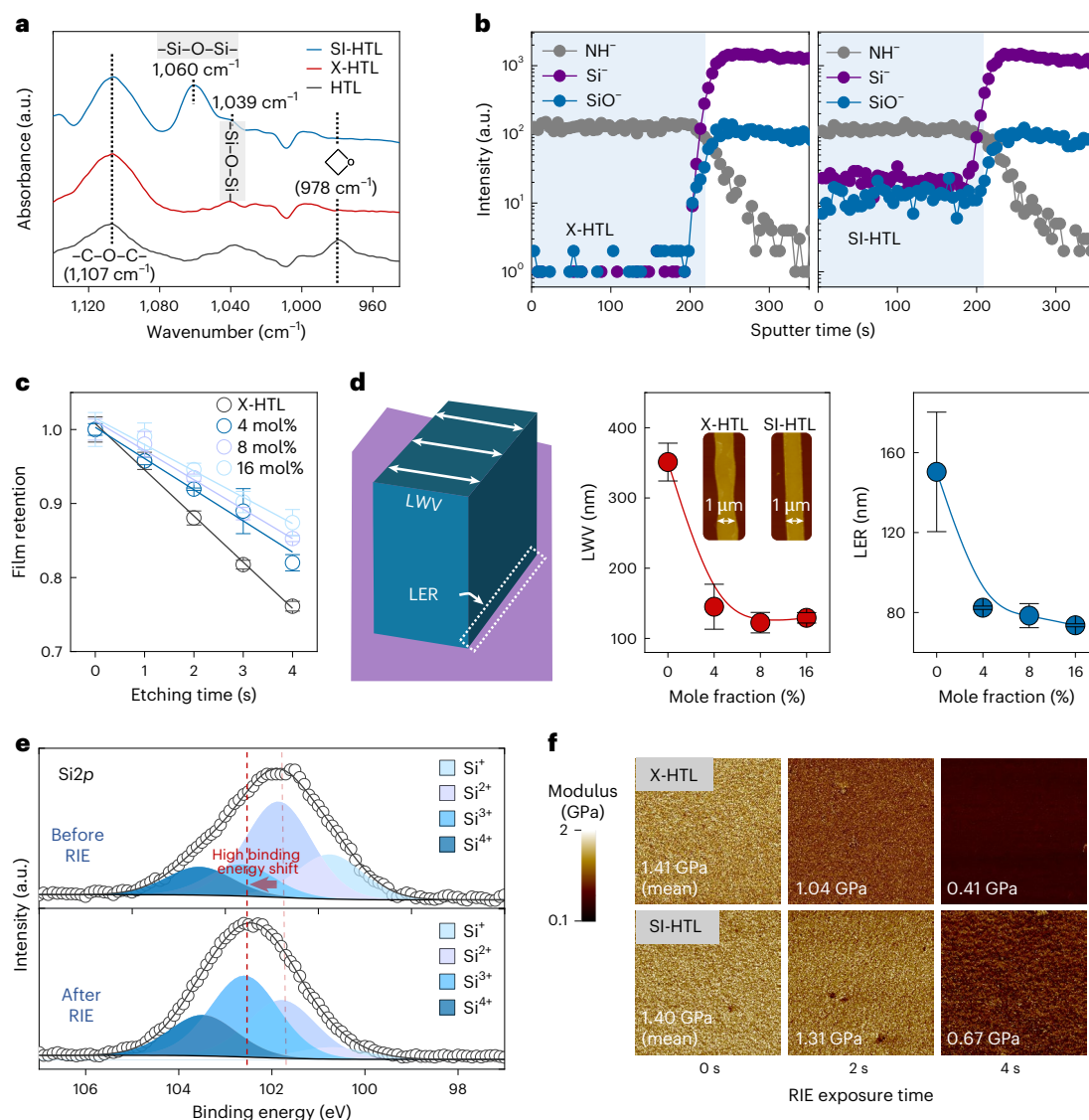


**Fig. 2 | Analysis of molecular structure and etch inhibitor of SI-HTL. a**, Fourier transform infrared spectra of HTL (before crosslinking), X-HTL (after crosslinking) and SI-HTL films. **b**, TOF-SIMS profiles of the X-HTL and SI-HTL films monitored over sputtering time. **c**, Film retention characteristics of X-HTL and SI-HTL films as a function of etching time. The indicated mol% value refers to the amount of silicone crosslinker relative to QUPD. The sample size ( $n$ ) used

to derive the statistics is 4. Mean values with  $\pm$  standard variations are indicated in the data. **d**, Evaluation of pattern fidelity in micro-patterns in terms of LWV and LER. The sample size ( $n$ ) used to derive the statistics is 3. Mean values with  $\pm$  standard variations are indicated in the data. **e**, XPS analysis of the surface regions of SI-HTL depending on RIE exposure. **f**, Surface modulus mapping images of X-HTL (top) and SI-HTL (bottom) films with various RIE exposure times.

the etch-inhibitor-based mechanism inherent to silicone materials is achievable in our small-molecule design of SI-HTL.

## Luminance characteristics of OLEDs based on SI-HTL

With the dry etching robustness and high-resolution patternability of SI-HTL, it is essential to retain its intrinsic HTL functionalities for the implementation of high-performance light-emitting devices. To explore the impact of SI-HTL on the electroluminescence (EL) characteristics, we fabricated OLEDs in the following configuration: indium tin oxide (ITO)/poly(3,4-ethylenedioxythiophene):poly(styrenesulfonate) (PEDOT:PSS) (40 nm)/X-HTL or SI-HTL (30 nm)/4,4'-bis(carbazol-9-yl) biphenyl:Tris(2-phenylpyridine)iridium(III) (CBP:Ir(ppy)<sub>3</sub>) (30 nm)/1,3,5-tris(1-phenyl-1-H-benzimidazol-2-yl)benzene (TPBi) (40 nm)/lithium fluoride (1.5 nm)/Al (150 nm) (Fig. 3a). Here PEDOT:PSS, CBP:Ir(ppy)<sub>3</sub> and TPBi are the hole injection layer, EML and electron transport layer, respectively. The incorporation of X-HTL resulted in improved OLED

performances, as shown in the current density–voltage–luminance ( $J$ – $V$ – $L$ ) curves, external quantum efficiency (EQE) and power efficiency (Supplementary Fig. 16). Figure 3b,c shows the  $J$ – $V$ – $L$  characteristics, EQE and current efficiency of SI-HTL-based OLEDs with varying concentrations of the silicone crosslinker. The detailed light-emitting performances are summarized in Supplementary Table 2. Interestingly, OLEDs integrated with SI-HTLs exhibited improved performance compared with those based on X-HTL. The EQEs and current efficiencies of SI-HTL-based OLEDs (made with 4 mol%, 8 mol% and 16 mol% of oxetane-based silicone crosslinker) were consistently higher than those of X-HTL-based OLEDs. Specifically, the EQE was 5.7% for OLEDs based on X-HTL and 6.9%, 6.9% and 6.6% for those based on SI-HTLs prepared with 4 mol%, 8 mol% and 16 mol% crosslinkers, respectively. The current efficiencies were 19.5 cd A<sup>-1</sup>, 23.6 cd A<sup>-1</sup>, 23.4 cd A<sup>-1</sup> and 22.5 cd A<sup>-1</sup> for the corresponding devices. Note that the performance of the OLEDs integrated with SI-HTL is comparable to—or even higher than—that of previously reported OLEDs using QUPD (Supplementary Table 3). In

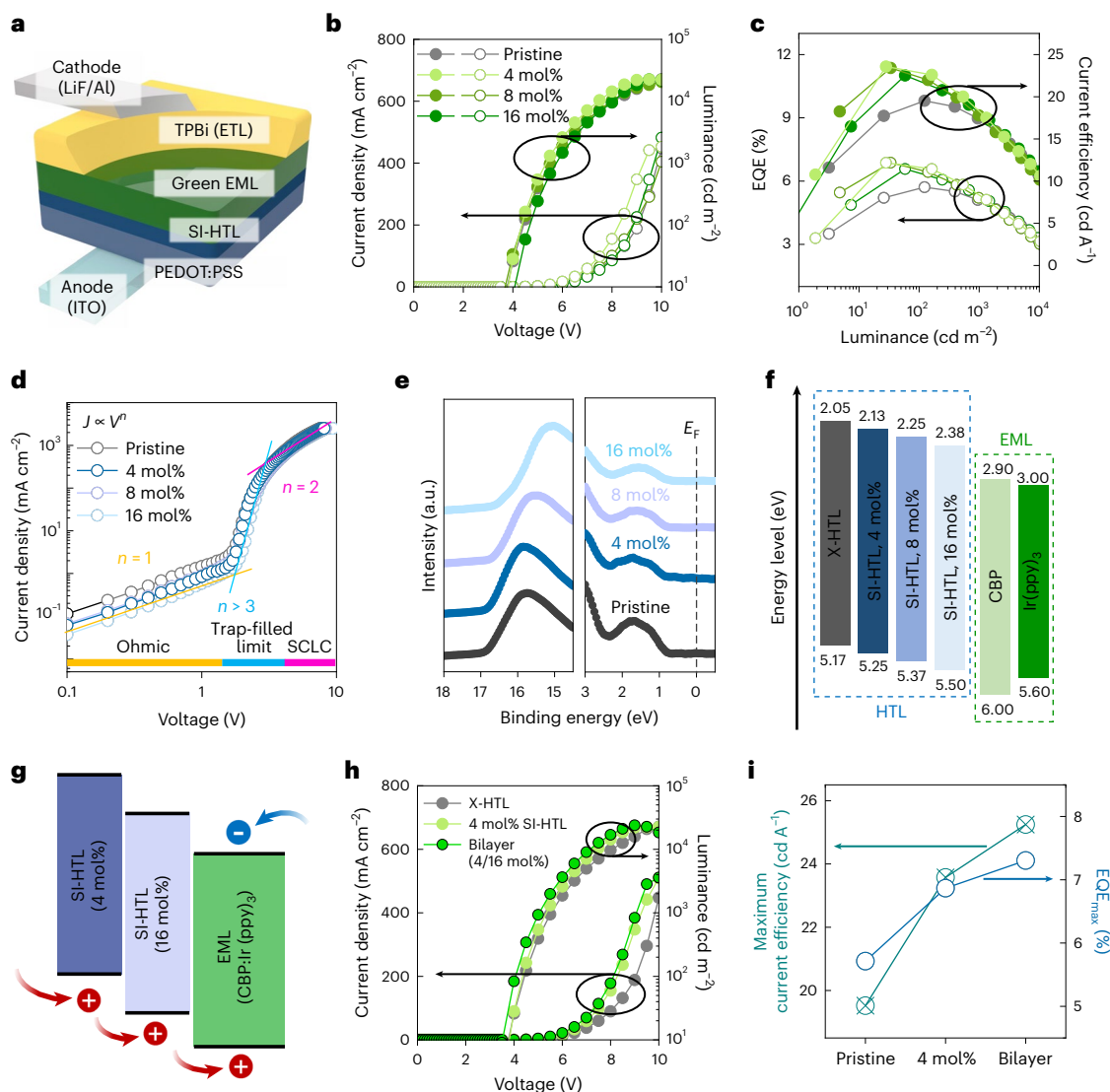


**Fig. 3 | EL characteristics of OLEDs integrated with SI-HTL. a**, Schematic of the device structure using SI-HTL as the HTL. **b**,  $J$ - $V$ - $L$  characteristics of OLEDs incorporating SI-HTL with various concentrations of silicone crosslinkers. **c**, EQE and current efficiency values of SI-HTL-based OLEDs plotted against luminance. **d**, SCLC characteristics of the hole-only devices utilizing SI-HTL. **e, f**, Ultraviolet photoelectron spectroscopy analysis and energy band diagram of SI-HTL films

with different silicone crosslinker concentrations. **g**, Energy band diagram of bilayer SI-HTL-based OLEDs. **h**, EL characteristics of the pristine, 4 mol% and bilayer SI-HTL-based OLEDs. **i**, Maximum current efficiency and maximum EQE extracted from the  $J$ - $V$ - $L$  measurement of pristine, 4 mol% and bilayer SI-HTL-based OLEDs. The x-marked circles and open circles correspond to the maximum current efficiency and maximum EQE, respectively.

addition, the enhanced efficiency of the device resulted in an improvement in the device lifetime (Supplementary Fig. 17).

To comprehend the underlying factors contributing to the enhancement in EL performance of the SI-HTL-integrated OLEDs, we conducted space-charge-limited current (SCLC) measurements to elucidate the hole mobility of SI-HTL (Fig. 3d). A hole-only device was fabricated with the configuration of ITO/PEDOT:PSS/SI-HTL/Al. The resulting  $J$ - $V$  curve exhibited the characteristic slope  $\left[\frac{d \log[J]}{d \log[V]}\right]$  of 1 under a low-voltage regime (ohmic); followed by a regime with a high slope ( $>3$ ), indicative of trap-filled limit; and last, an SCLC regime characterized by a slope of 2. The hole mobility for the hole-only device was calculated using the Mott–Gurney equation:  $J = \frac{9}{8} \epsilon \epsilon_0 \mu \frac{(V - V_{bi})^2}{L^3}$  where  $\epsilon$ ,  $\epsilon_0$ ,  $V_{bi}$ ,  $L$  and  $\mu$  are the dielectric constant, permittivity of free space, a built-in voltage, thickness of HTL films and hole mobility, respectively. As a result, the hole mobility value for pristine X-HTL was found to be  $4.4 \times 10^{-6} \text{ cm}^2 \text{ V}^{-1} \text{ s}^{-1}$ , whereas those for SI-HTLs based on 4 mol%, 8 mol% and 16 mol% of silicone crosslinkers were extracted to be

$4.1 \times 10^{-6} \text{ cm}^2 \text{ V}^{-1} \text{ s}^{-1}$ ,  $3.8 \times 10^{-6} \text{ cm}^2 \text{ V}^{-1} \text{ s}^{-1}$  and  $3.6 \times 10^{-6} \text{ cm}^2 \text{ V}^{-1} \text{ s}^{-1}$ , respectively (Supplementary Fig. 18). The observed slight decrease in hole mobility can be attributed to the inclusion of insulating silicone blocks, as evidenced by the increased trap densities and photoluminescence quenching effects in SI-HTLs (Supplementary Figs. 18 and 19). Despite the reduced mobility of the layer, the improved efficiency of the devices based on SI-HTL can be understood in terms of the balance between electron and hole transport. Considering that the hole mobility ( $2 \times 10^{-3} \text{ cm}^2 \text{ V}^{-1} \text{ s}^{-1}$ ) of CBP (that is, the host material of the EML) is higher than its electron mobility ( $3 \times 10^{-4} \text{ cm}^2 \text{ V}^{-1} \text{ s}^{-1}$ ) (ref. 41), the reduction in the hole mobility of SI-HTL can adversely contribute to balancing the hole–electron transport in the EML<sup>12,42,43</sup>, thereby improving the luminance performance.

In conjunction with the charge transport characteristics of SI-HTL, its energy level needs to be explored to fully understand its influence on the luminance performance in OLEDs. To characterize the electronic structures of SI-HTL after the introduction of the silicone crosslinker, ultraviolet photoelectron spectroscopy was conducted (Fig. 3e).

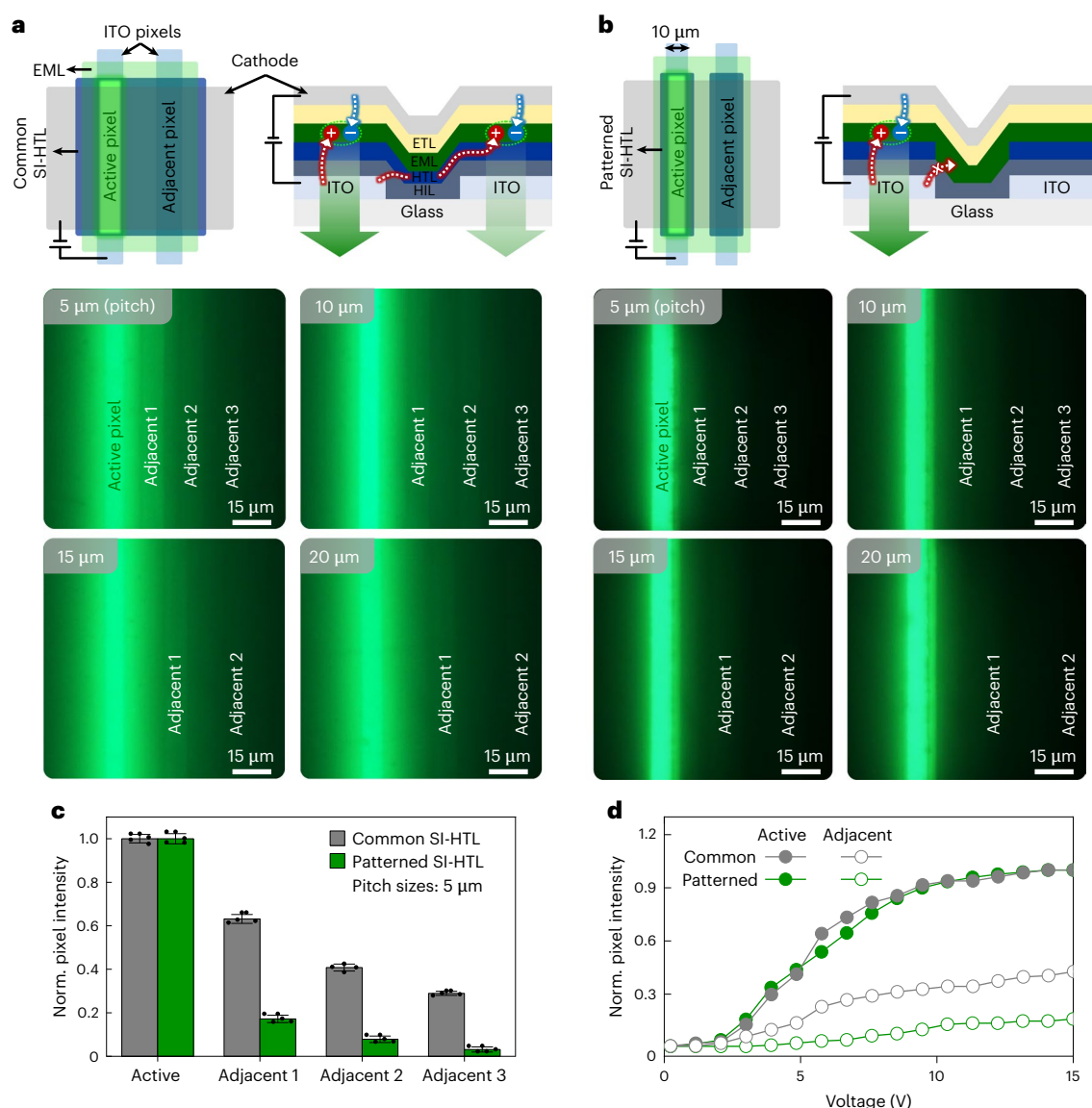


**Fig. 4 | Evaluation of electrical pixel crosstalk in OLEDs with micro-patterned SI-HTL.** **a, b**, Top-view and side-view schematics of OLEDs featuring patterned anode pixels using common SI-HTL (**a**) and micro-patterned SI-HTL (**b**) (top), accompanied by optical microscopy images (bottom) of varying pitch sizes to demonstrate crosstalk emission on the active pixel. HIL, hole injection layer. **c**,

Normalized green-pixel intensities extracted from the OLEDs integrated with common and patterned SI-HTLs. The sample size ( $n$ ) used to derive the statistics is 4. Mean values with  $\pm$  standard variations are indicated in the data. **d**, Voltage-dependent normalized green-pixel intensities derived from the adjacent pixel (Adjacent 2) in the OLEDs integrated with common and patterned SI-HTLs.

The calculated HOMO energy level for X-HTL was 5.17 eV from the vacuum level, whereas those for SI-HTL crosslinked using 4 mol%, 8 mol% and 16 mol% silicone crosslinker were 5.25 eV, 5.37 eV and 5.50 eV, respectively. Combined with the optical bandgap obtained from the Tauc plot of ultraviolet–visible absorption spectra (Supplementary Fig. 20), the energy band diagrams of these films were determined (Fig. 3f). We conjecture that the downshift in the HOMO (and lowest unoccupied molecular orbital) may be attributed to the presence of silanol groups (Si–OH) in the bulk of the SI-HTL film, which did not participate in the sol–gel reactions<sup>36,44</sup> (Supplementary Fig. 21); the electron-withdrawing property of the silanol groups can induce a stabilization of the molecular orbitals<sup>45,46</sup>. The deeper HOMO level of SI-HTL provides favourable energy level alignment with the EML, facilitating efficient hole injection into the EML film. However, the accompanying lower lowest unoccupied molecular orbital level of SI-HTL weakens its electron-blocking characteristic. Consequently, we consider that the delicate optimization in the energy levels of SI-HTL,

along with its altered hole mobility, led to the highest performance in devices based on SI-HTL prepared with 4 mol% silicone crosslinker. On the basis of this, despite the minimal variation in the luminance efficiency of the OLEDs integrated with SI-HTLs (4 mol%, 8 mol% and 16 mol%), we optimized the amount of silicone crosslinker to 4 mol% to achieve the highest efficiency among them.

Furthermore, the chemical robustness and the ability to control the HOMO level of SI-HTL are advantageous for realizing multilayered HTL-based OLEDs that exploit enhanced energy level alignment. To this end, we fabricated bilayered SI-HTLs—with SI-HTL using 4 mol% crosslinker in the bottom layer and 16 mol% crosslinker in the top, with different thickness ratios (25:75, 50:50 and 75:25)—that can produce a gradient energy landscape facilitating hole injections into the EML (Fig. 3g). In particular, the OLED with bilayered SI-HTLs (with a 1:1 thickness ratio between the bottom and top layers) demonstrated improved luminous characteristics compared with devices based on both X-HTL and single-layered SI-HTL (Fig. 3h,i and Supplementary Figs. 22 and 23).



This indicates that SI-HTL can effectively modulate charge transport and injection into the EML, enhancing the OLED performance.

## Evaluation of electrical pixel crosstalk effect

The demonstrated ultrafine pixelation and improved HTL functionalities of SI-HTL have the potential to realize highly efficient, anti-pixel-crosstalk OLEDs (Fig. 1a,c). To evaluate the electrical pixel crosstalk depending on the pixelation of HTLs, we designed OLED configurations with varying ITO pixel pitches (5  $\mu\text{m}$ , 10  $\mu\text{m}$ , 15  $\mu\text{m}$  and 20  $\mu\text{m}$ ) (Supplementary Fig. 24), in which either an unpatterned common SI-HTL was used (Fig. 4a) or the SI-HTL was pixelated corresponding to the size of the ITO pixel pitches (Fig. 4b). The other OLED layer configurations were identical to those in Fig. 3. Note that during the deposition and photolithography patterning of SI-HTL, the characteristics of the underlying hole injection layer remained intact, despite exposure to processing solvents (Supplementary Fig. 25). In both device configurations, a voltage bias was swept from 0 V to 15 V between the anode of the active pixel and the shared cathode, as well as ensuring the anodes of the adjacent pixels remained open-circuited. In all pixel pitches within the common SI-HTL case, light emission from the adjacent pixels were observed, most apparently for the test devices with 5  $\mu\text{m}$  pixel pitches (Fig. 4a). This light emission originated from parasitic electric currents travelling from the active anode to the common SI-HTL and finally to the shared cathode of neighbouring pixels (Fig. 1b). Conversely, the pixel crosstalk phenomenon was greatly reduced in the patterned SI-HTL device at all pixel pitches (Fig. 4b and Supplementary Video 1). Even for the test devices with 5  $\mu\text{m}$  pixel pitch, the pixel intensities of adjacent pixels were substantially diminished compared with that in the devices based on common SI-HTL (Fig. 4c and Supplementary Fig. 26). Figure 4d shows the voltage-dependent green-pixel intensities of the active pixel and adjacent pixel (Fig. 4, Adjacent 2) of both OLEDs using common SI-HTL and pixelated SI-HTL, further validating the effectiveness of SI-HTL pixelation in reducing the crosstalk emission. Nevertheless, we acknowledge a small parasitic intensity observable even in the adjacent pixels of the pixelated SI-HTL OLEDs. We did not attribute the finite crosstalk emission to the electrical pixel crosstalk caused by lateral leakage currents through the common hole injection layer we used (Supplementary Figs. 27–29 and Supplementary Note 3). Instead, it could be attributable to combinations of electrical crosstalk through the common EML we used (which can, in future, be prevented by pixelating EML) and optical effect (light diffusion or scattering). The lateral leakage currents of both active pixel and adjacent pixel (Fig. 4, Adjacent 1) on sweeping the voltage bias of the active pixel—for testbed devices in common and patterned SI-HTL configurations—are shown in Supplementary Fig. 28a. Clearly, the parasitic current collected from the anode of the adjacent pixel was lower, by nearly an order of magnitude, for devices with patterned SI-HTL than devices with common SI-HTL (Supplementary Fig. 28b). Supplementary Figs. 28c and 30 show the lateral leakage current of adjacent pixel 1 for each pixel pitch configuration at a constant voltage bias of 8 V. The lateral leakage currents in OLEDs with patterned SI-HTL were substantially decreased across all pixel pitches, compared with those with common SI-HTL. Consequently, these results indicate that the efficacy of SI-HTL patterning is an effective strategy to mitigate the crosstalk effect.

## Conclusions

We have reported a silicone-integrated small-molecule HTL that can be patterned using photolithography and RIE processes. The embedded silicone network within the s-OSC matrix allows the SI-HTL to be micro-patterned with high fidelity by emulating the anisotropic etching characteristics of silicon materials. Furthermore, the SI-HTL exhibited enhanced luminance efficiency in OLEDs, which is attributed to the modulation of charge-transporting capability and the optimized alignment of energy levels relative to those of the emissive layer. The

SI-HTL, therefore, exhibits both high-resolution patternability and enhanced electronic HTL functionality. We used the approach to create high-density pixelation of the HTL up to 10,062 ppi on a wafer scale. The accurate pixelation of the SI-HTL effectively reduces the electrical pixel crosstalk in the OLED. Our materials-based approach could be of use in the development of high-density microdisplay technology as well as potentially be applied to optoelectronic materials beyond small-molecule organics, such as quantum dots and perovskites.

## Methods

### Materials

Processing solvents including chlorobenzene were purchased from Sigma-Aldrich and were used as received. QUPD, OTPD, X-F6-TAPC, Ox-DCEPA (The full chemical names of the materials are provided in Supplementary Fig. 2) and bifunctionalized silicone crosslinker (trithoxy[3-[(3-ethyl-3-oxetanyl)methoxy]propyl]silane) were provided by Lumtec and JSI Silicone. PEDOT:PSS (AI4083) was purchased from Ossila. The photoinitiator, (4-(octyloxy)phenyl)(phenyl)iodonium hexafluorostibate(v), was purchased from AmBeed. CBP and Ir(ppy)<sub>3</sub> were purchased from TCI Chemicals. TPBi and lithium fluoride were purchased from Sigma-Aldrich. Al pellets ( $\geq 99.999\%$ ) were purchased from Taewon Science. Glass substrate with a prepatterned ITO electrode ( $\sim 20 \Omega \text{ sq}^{-1}$ ) was purchased from AMG. The photoresist (KL 5302) and developer (AZ 300MIF) were purchased from NM Tech and AZ Electronic Materials, respectively.

### Preparation and characterization of SI-HTL film

The PEDOT:PSS was spin coated at 4,000 r.p.m. for 1 min onto a SiO<sub>2</sub> or ITO/glass substrate and was annealed at 120 °C for 1 h. A solution of SI-HTL was prepared by dissolving QUPD (10 mg ml<sup>-1</sup> in chlorobenzene) and silicone crosslinkers (4 mol%, 8 mol% and 16 mol% relative to QUPD), and was mixed at 100 °C for 2 h. After mixing, the solution was spin coated at 2,000 r.p.m. for 1 min onto the prepared PEDOT:PSS-coated substrate, and then the resulting film was annealed at 180 °C for 3 h in a N<sub>2</sub> environment. During the annealing process, the oxetane ring-opening reaction was activated by protonation from the underlying PEDOT:PSS or (4-(octyloxy)phenyl)(phenyl)iodonium hexafluorostibate(v) (refs. 47,48). Concurrently, the sol-gel reaction between the silicone crosslinkers was driven by thermal energy<sup>28,36</sup>. The thickness of the films was measured by a surface profilometer (Bruker, Dektak XT-E) and atomic force microscope (Park Systems, NX10). The oxetane ring-opening reaction and formation of silicone network were confirmed by Fourier transform infrared spectroscopy (Thermo Fisher Scientific, Nicolet iS50). The TOF-SIMS analysis was performed with a TOF SIMS-5 (IONTOF) instrument. The surface morphology and height profile of the patterned SI-HTL films were characterized using the atomic force microscope in the non-contact mode under ambient conditions. The cross-sectional TEM samples were obtained by focused ion beam (Helios 650), and the TEM analysis was conducted with a Cs-corrected scanning TEM instrument (JEM-ARM200F) at the National Center of Inter-University Research Facilities. The pattern fidelity of the micro-patterned SI-HTL films was evaluated by statistically analysing the atomic force microscope images with ImageJ 1.51k software. The surface modulus and mapping images were obtained using probes from Park Systems (PPP-FMR; resonant frequency,  $\sim 75 \text{ kHz}$ ; spring constant,  $k = -2.8 \text{ N m}^{-1}$ ; tip radius, 8  $\mu\text{m}$ ). XPS measurements were performed by a Theta Probe Base system (Thermo Fisher Scientific). Ultraviolet absorption and photoluminescence spectra of SI-HTL films were measured by a ultraviolet-visible-near-infrared spectrophotometer (Jasco V-770) and fluorescence spectrometer (SCINCO, FS-2), respectively. Ultraviolet photoelectron spectroscopy measurements were performed using an XPS system (Thermo Fisher Scientific, XPS Theta Probe). A negative bias voltage ( $-10 \text{ eV}$ ) was applied to the samples using He(I) (21.2 eV) as the excitation source. The SCLC measurements on hole-only devices were conducted using a Keithley 4200A-SCS

instrument. The voltage was incrementally swept from 0.1 V to 9 V on ITO, with a step size of 0.1 V.

### Fabrication and performance measurement of OLED

An ITO-patterned glass substrate was sonicated with acetone, isopropyl alcohol and deionized water sequentially for 15 min each. The cleaned substrate was treated with ultraviolet/ozone for 20 min. PEDOT:PSS (AI4083) was spin coated onto the ITO-patterned glass substrate at 4,000 r.p.m. for 1 min and the resulting film was annealed at 150 °C for 30 min under ambient conditions. The prepared QUPD or SI-HTL solutions were spin coated onto the PEDOT:PSS film in a N<sub>2</sub>-filled glove box at 2,000 r.p.m. for 60 s, followed by thermal annealing at 180 °C for 3 h. Next, the EML (CBP:Ir(ppy)<sub>3</sub>) was spin coated onto the HTL films, followed by thermal annealing at 60 °C for 10 min. Then, 40 nm TPBi was thermally evaporated through a shadow mask under a high vacuum ( $2.0 \times 10^{-6}$  torr). Last, 1.5 nm lithium fluoride and 150 nm Al as the cathode electrode were thermally evaporated through a shadow mask under the high-vacuum condition ( $2.0 \times 10^{-6}$  torr). The EL performance of the OLED was evaluated by a spectroradiometer (CS-2000, Konica Minolta), and the input voltage was swept from 0 V to 12 V using a Keithley 2400 SCS.

### Patterning of the SI-HTL film and evaluation of pixel crosstalk

A glass substrate was cleaned as previously described. The photoresist (KL 5302) was spin coated at 4,000 r.p.m. for 1 min onto the substrate, and then soft baking was conducted at 105 °C for 1 min. The photoresist-coated substrate was exposed to the ultraviolet source ( $365 \text{ nm}$ ,  $25 \text{ mW cm}^{-2}$ ) for 2 s with a photomask using a mask aligner (Pro Win M-150), and post-baking was followed at 115 °C for 1 min. The photoresist pattern was developed using the developer for 20 s at room temperature. After the conventional photolithography process, a 50-nm-thick ITO layer was sputtered onto the photoresist pattern layer using radio-frequency magnetron sputtering. Finally, the photoresist pattern layer was removed by sonication with acetone for 5 min, resulting in ITO patterns. Both PEDOT:PSS and SI-HTL were then sequentially deposited using the previously described process onto the patterned ITO glass. For micro-patterning of the SI-HTL films, the photoresist was patterned by the above-described photolithography process. The photoresist-patterned SI-HTL films were dry etched with RIE (JVAC JVR1E-8AT). The films were exposed to Ar/O<sub>2</sub> (40 s.c.c.m./20 s.c.c.m.) etching gas mixture for 20–30 s, using 50 W radio-frequency power at a pressure below 0.1 mtorr. Subsequently, the patterned photoresist was stripped using a sonication process with acetone and isopropyl alcohol, resulting in the formation of SI-HTL micro-patterns. Pixel crosstalk was observed by an optical microscope (ECLIPSE LV100ND, Nikon) and applying voltages through a d.c. power supply. The crosstalk currents were measured using a Keithley 4200A-SCS instrument.

### Data availability

The data that support the findings of this study are available from the corresponding authors upon reasonable request.

### References

- Joo, W.-J. & Brongersma, M. L. Creating the ultimate virtual reality display. *Science* **377**, 1376–1378 (2022).
- Zhan, T., Yin, K., Xiong, J., He, Z. & Wu, S. T. Augmented reality and virtual reality displays: perspectives and challenges. *iScience* **23**, 101397 (2020).
- Xiong, J. H. et al. Augmented reality and virtual reality displays: emerging technologies and future perspectives. *Light Sci. Appl.* **10**, 216 (2021).
- Ha, J. et al. Advanced VR and AR displays: improving the user experience. *J. Soc. Inf. Disp.* **39**, 15–19 (2023).
- Kang, C.-M. & Lee, H. Recent progress of organic light-emitting diode microdisplays for augmented reality/virtual reality applications. *J. Inf. Disp.* **23**, 19–32 (2022).
- Diethelm, M. et al. Quantitative analysis of pixel crosstalk in AMOLED displays. *J. Inf. Disp.* **19**, 61–69 (2018).
- Kang, H. et al. Investigating the electrical crosstalk effect between pixels in high-resolution organic light-emitting diode microdisplays. *Sci. Rep.* **13**, 14070 (2023).
- Engelhart, J. et al. Hole-transport materials—key enablers for future OLED display evolution. *SID Symp. Dig. Tech. Pap.* **53**, 877–880 (2022).
- Braga, D. et al. Modeling electrical and optical cross-talk between adjacent pixels in organic light-emitting diode displays. *SID Symp. Dig. Tech. Pap.* **50**, 31–34 (2019).
- Kaçar, R., Serin, R. B., Uçar, E. & Ülkü, A. Removing crosstalk effect for high efficient polymer light emitting diode display. *Solid State Electron.* **192**, 108253 (2022).
- Lee, J.-M. et al. Analysis and simulation of reddish overshoot in active matrix organic light-emitting diode display with varying p-doped hole transport layer concentrations. *Org. Electron.* **99**, 106328 (2021).
- Swayamprabha, S. S. et al. Hole-transporting materials for organic light-emitting diodes: an overview. *J. Mater. Chem. C* **7**, 7144–7158 (2019).
- Cha, S. & Kim, C. Transfer-printing phosphorescent OLEDs: progress towards microdisplay applications. *Org. Electron.* **122**, 106891 (2023).
- Jo, P. S., Vailionis, A., Park, Y. M. & Salleo, A. Scalable fabrication of strongly textured organic semiconductor micropatterns by capillary force lithography. *Adv. Mater.* **24**, 3269–3274 (2012).
- Bae, I. et al. Tailored single crystals of triisopropylsilyl ethynyl pentacene by selective contact evaporation printing. *Adv. Mater.* **23**, 3398–3402 (2011).
- Skhunov, M. et al. Pixelated full-colour small molecule semiconductor devices towards artificial retinas. *J. Mater. Chem. C* **9**, 5858–5867 (2021).
- Bail, R., Hong, J. Y. & Chin, B. D. Inkjet printing of blue phosphorescent light-emitting layer based on bis(3,5-di(9H-carbazol-9-yl))diphenylsilane. *RSC Adv.* **8**, 11191–11197 (2018).
- Zhou, X. et al. Dewetting-assisted patterning of organic semiconductors for micro-OLED arrays with a pixel size of 1 μm. *Small Methods* **6**, 2101509 (2022).
- Zhu, J. et al. Micro organic light-emitting diodes fabricated through area-selective growth. *Mater. Chem. Front.* **1**, 2606–2612 (2017).
- Jiang, Y., Tam, B. S. T., Dong, S.-C. & Tang, C. W. 2-inch, 2,000-ppi silicon nitride mask for patterning ultra-high-resolution OLED displays. *SID Symp. Dig. Tech. Pap.* **51**, 909–912 (2020).
- Kajiyama, Y., Joseph, K., Kajiyama, K., Kudo, S. & Aziz, H. Small feature sizes and high aperture ratio organic light-emitting diodes by using laser-patterned polyimide shadow masks. *Appl. Phys. Lett.* **104**, 053303 (2014).
- Jung, J. H. et al. Enhancement of luminance efficiency of 3,000 ppi OLED micro-display using RGB direct patterning. *SID Symp. Dig. Tech. Pap.* **54**, 217–220 (2023).
- Yamane, Y. et al. 3207-ppi, 1.50-in. OLED microdisplay with all pixels formed through RGB side-by-side patterning by photolithography. *SID Symp. Dig. Tech. Pap.* **54**, 1334–1337 (2023).
- Malinowski, P. E. et al. Photolithography as enabler of AMOLED displays beyond 1,000 ppi. *SID Symp. Dig. Tech. Pap.* **48**, 623–626 (2017).
- Malinowski, P. E. et al. Multicolor 1,250 ppi OLED arrays patterned by photolithography. *SID Symp. Dig. Tech. Pap.* **47**, 1009–1012 (2016).
- Joo, W.-J. et al. Metasurface-driven OLED displays beyond 10,000 pixels per inch. *Science* **370**, 459–463 (2020).



27. Kim, C. et al. Fine metal mask material and manufacturing process for high-resolution active-matrix organic light-emitting diode displays. *J. Soc. Inf. Disp.* **28**, 668–679 (2020).
28. Kweon, H. et al. Silicone engineered anisotropic lithography for ultrahigh-density OLEDs. *Nat. Commun.* **13**, 6775 (2022).
29. Murawski, C., Fuchs, C., Hofmann, S., Leo, K. & Gather, M. C. Alternative p-doped hole transport material for low operating voltage and high efficiency organic light-emitting diodes. *Appl. Phys. Lett.* **105**, 113303 (2014).
30. Zhou, X. et al. Enhanced hole injection into amorphous hole-transport layers of organic light-emitting diodes using controlled p-type doping. *Adv. Funct. Mater.* **11**, 310–314 (2001).
31. Zhang, X. et al. Highly-efficient low-voltage organic light-emitting diode by controlling hole transporting with doped dual hole-transport layer and the impedance spectroscopy analysis. *Synth. Met.* **205**, 134–138 (2015).
32. Yadav, R. A. K., Dubey, D. K., Chen, S.-Z., Liang, T.-W. & Jou, J.-H. Role of molecular orbital energy levels in OLED performance. *Sci. Rep.* **10**, 9915 (2020).
33. Dou, J.-H. et al. Organic semiconducting alloys with tunable energy levels. *J. Am. Chem. Soc.* **141**, 6561–6568 (2019).
34. Aizawa, N. et al. Solution-processed multilayer small-molecule light-emitting devices with high-efficiency white-light emission. *Nat. Commun.* **5**, 5756 (2014).
35. Park, S., Kilgallon, L. J., Yang, Z., Ryu, D. Y. & Ryu, C. Y. Molecular origin of the induction period in photoinitiated cationic polymerization of epoxies and oxetanes. *Macromolecules* **52**, 1158–1165 (2019).
36. Park, H. W. et al. Universal route to impart orthogonality to polymer semiconductors for sub-micrometer tandem electronics. *Adv. Mater.* **31**, 1901400 (2019).
37. Yang, J. et al. Nondestructive photopatterning of heavy-metal-free quantum dots. *Adv. Mater.* **34**, 2205504 (2022).
38. Mehonic, A. et al. Structural changes and conductance thresholds in metal-free intrinsic SiO<sub>x</sub> resistive random access memory. *J. Appl. Phys.* **117**, 124505 (2015).
39. Bashouti, M. Y., Sardashti, K., Ristein, J. & Christiansen, S. Kinetic study of H-terminated silicon nanowires oxidation in very fast stages. *Nanoscale Res. Lett.* **8**, 41 (2013).
40. Louis, B., Caubergh, S., Larsson, P.-O., Tian, Y. & Scheblykin, I. G. Light and oxygen induce chain scission of conjugated polymers in solution. *Phys. Chem. Chem. Phys.* **20**, 1829–1837 (2018).
41. Kang, J.-W. et al. Low roll-off of efficiency at high current density in phosphorescent organic light emitting diodes. *Appl. Phys. Lett.* **90**, 223508 (2007).
42. Cha, S. W., Joo, S.-H., Jeong, M.-H. & Jin, H.-I. Balancing charge carrier mobility by constructing chemical structures to contain both hole- and electron-transporting moieties in electroluminescent organic compounds. *Synth. Met.* **150**, 309–316 (2005).
43. Liao, C.-H., Lee, M.-T., Tsai, C.-H. & Chen, C. H. Highly efficient blue organic light-emitting devices incorporating a composite hole transport layer. *Appl. Phys. Lett.* **86**, 203507 (2005).
44. Kim, J. et al. Interpenetrating polymer semiconductor nanonetwork channel for ultrasensitive, selective, and fast recovered chemodetection. *ACS Appl. Mater. Interfaces* **12**, 55107–55115 (2020).
45. Chua, L.-L. et al. General observation of n-type field-effect behaviour in organic semiconductors. *Nature* **434**, 194–199 (2005).
46. Brunner, K. et al. Carbazole compounds as host materials for triplet emitters in organic light-emitting diodes: tuning the HOMO level without influencing the triplet energy in small molecules. *J. Am. Chem. Soc.* **126**, 6035–6042 (2004).
47. Köhnen, A. et al. The simple way to solution-processed multilayer OLEDs—layered block-copolymer networks by living cationic polymerization. *Adv. Mater.* **21**, 879–884 (2009).
48. Tsai, K.-W., Hung, M.-K., Mao, Y.-H. & Chen, S.-A. Solution-processed thermally activated delayed fluorescent OLED with high EQE as 31% using high triplet energy crosslinkable hole transport materials. *Adv. Funct. Mater.* **29**, 1901025 (2019).

## Acknowledgements

D.H.K. acknowledges support from the Basic Science Research Program (2020R1A2C3014237 and RS-2024-00405818) and the Pioneer Research Center Program (2022M3C1A3081211) of the National Research Foundation of Korea (NRF) funded by the Ministry of Science and ICT, Korea and the Technology Innovation Program (RS-2024-00441743) funded by the Ministry of Trade, Industry & Energy (MOTIE, Korea). M.S.K. acknowledges support from the Basic Science Research Program (2021R1A2C2008332) and the Nano & Material Technology Development Program (RS-2024-00445116) of the NRF funded by the Ministry of Science and ICT, Korea.

## Author contributions

M.S.K., J.H.C. and D.H.K. supervised this project. H.K., B.H. and D.H.K. conceived the concept. H.K., S.K. and B.H. designed and carried out the experiments. H.K., B.H., So.L., S.H.R., J.H. and D.H.K. analysed the molecular structure and etching behaviour of SI-HTL. H.K. and B.H. fabricated the high-resolution patterns of SI-HTL. S.K., Se.L., M.K., S.H.R., M.S.K. and J.H.C. evaluated and interpreted the optoelectronic characteristics of SI-HTL and OLEDs. H.K., S.K. and H.O. fabricated and evaluated the pixel crosstalk of patterned SI-HTL-based OLEDs. All authors discussed the results and commented on the paper. H.K., S.K., B.H., M.S.K., J.H.C. and D.H.K. co-wrote the paper.

## Competing interests

H.K., S.K., B.H., Se.L., M.S.K., J.H.C. and D.H.K. declare their status as inventors on the granted Korean patent (KR 10-2537611) and have filed the patent application (PCT/KR2023/009730). Additionally, H.K., B.H. and D.H.K. declare their status as inventors on the granted Korean patent (KR 10-2547153) and have filed the patent application (PCT/KR2023/002902). The other authors declare no competing interests.

## Additional information

**Supplementary information** The online version contains supplementary material available at <https://doi.org/10.1038/s41928-024-01327-5>.

**Correspondence and requests for materials** should be addressed to Moon Sung Kang, Jeong Ho Cho or Do Hwan Kim.

**Peer review information** *Nature Electronics* thanks Ching-Fuh Lin, Alper Ulku and the other, anonymous, reviewer(s) for their contribution to the peer review of this work.

**Reprints and permissions information** is available at [www.nature.com/reprints](http://www.nature.com/reprints).

**Publisher's note** Springer Nature remains neutral with regard to jurisdictional claims in published maps and institutional affiliations.

Springer Nature or its licensor (e.g. a society or other partner) holds exclusive rights to this article under a publishing agreement with the author(s) or other rightsholder(s); author self-archiving of the accepted manuscript version of this article is solely governed by the terms of such publishing agreement and applicable law.

© The Author(s), under exclusive licence to Springer Nature Limited 2025